Biointerface Research in Applied Chemistry
Open-Access Journal (ISSN: 2069-5837)

Article
Volume 13, Issue 3, 2023, 274
https://doi.org/10.33263/BRIAC133.274

Synthesis and Characterization of Biocomposite Films of Methylcellulose-Based with Nanocellulose

Sobnom Mustary [1,*], Marianne Odlyha [1], Asraful Alam [2], Mohammed Anowar Hosen [2], Md Simul Bhuyan [3], Imtiaj Hasan [4], Sarkar M. A. Kawsar [2,*]

1 Department of Biological Sciences, Birkbeck, University of London, United Kingdom
2 Laboratory of Carbohydrate and Nucleoside Chemistry (LCNC), Department of Chemistry, Faculty of Science, University of Chittagong, Chittagong-4331, Bangladesh
3 Bangladesh Oceanographic Research Institute (BORI), Cox's Bazar, Bangladesh
4 Department of Biochemistry and Molecular Biology, University of Rajshahi, Rajshahi-6205, Bangladesh
* Correspondence: akawsar@cu.ac.bd; (S.M.A.K.); sobnom99@gmail.com (S.M)

Scopus Author ID 24334966300
Received: 6.04.2022; Accepted: 21.06.2022; Published: 10.07.2022

Abstract: This study explores the development of nontoxic biocomposite films from methylcellulose (MC) and crystalline nanocellulose (CNC). First, a methylcellulose sample (Tylose MH 50) of concentration 1.5% (w/w) and crystalline nanocellulose type-1 samples of different concentrations were prepared to obtain these biocomposite films. Films were then produced by adjusting methylcellulose solution with nanocellulose solution following the casting-evaporation methodology. The molecular interactions of crystalline nanocellulose with methylcellulose were investigated using ATR Fourier Transform Infrared (FTIR) spectroscopy. FTIR analysis of films revealed a shift of absorption peak in the region of 3200-3600 cm^{-1} to a lower value and found an intense peak at 1031 cm^{-1} with the incorporation of CNC into Tylose MH 50 film. The thermal stability of these films was examined using thermogravimetric analysis (TGA), indicating the films' higher stability than MC. Mechanical properties were measured by controlled RH by dynamic mechanical analysis (DMA), showing changes in Young's modulus from the initial slope of stress-strain plots and storage modulus (E′) as the concentration of CNC increased in films. The data were obtained from bionanocomposite films, which were not even with variations in thickness as measured by a digital micrometer. The mechanical properties of bionanocomposite films showed variation due to the varying local orientation of CNCs in MC, as it contradicts work that was previously done in this area which suggests a uniform orientation of CNCs in MC biopolymer. Further research on these biocomposite films is expected to find more significant uses.

Keywords: biocomposite; methylcellulose; nanocellulose; nanocomposite film; tensile strength.

1. Introduction

The increasing interest in using biopolymer and biocomposite materials for environmental safety led the researcher to develop newer sustainable, biodegradable polymers [1]. Biodegradable packaging materials are produced from renewable biological raw materials such as starch, chitosan, agar, cellulose, etc. [2-7]. Among them, cellulose is the most available natural biopolymer on the earth and is largely used for preparing composites with other biopolymers [8-12]. On the other hand, synthetic polymers have excellent thermomechanical properties like strength, durability, flexibility, and heat resistance. Still, they cannot meet sustainable demands due to limited supplies of non-renewable petroleum polyolefins

(polyethylene and polypropylene) [13-16]. Moreover, biopolymer's advantages over synthetic polymers as synthetic ones continuously add solid waste products to the environment.

Methylcellulose (MC) is a cellulose derivative and can be synthesized from wood, cotton, and plant pulps. MC is also called cellulose ether [17]. It has a chemical structure, as shown in Figure 1. Partial replacement of the hydroxyl groups in cellulose with methyl groups produces MC. MC is modified water-soluble cellulose used as a matrix for biomedical and biodegradable nanocomposites. It is a biodegradable, biocompatible, and non-cytotoxic polymer with excellent film-forming properties. It can be used in pharmaceuticals, foods, agricultural products, construction materials, paints, ceramics, detergents, adhesives, and cosmetics [18-25]. The compatibility of MC with CNC was good because of the interaction between OH groups in the nanocomposite, which gives H-bond a cross-linked structure (Figure 1). MC films have weak mechanical properties, high water sensitivity, and poor barrier properties.

Among them, blending polymers with fillers (reinforcing) is the most efficient way to modify the properties of polymers with different amounts of fillers [26]. Films produced from the blending of biopolymers usually exhibit modified properties compared to films made from an individual component [27-29]. Among them, nanosize fillers are useful reinforcing agents [30].

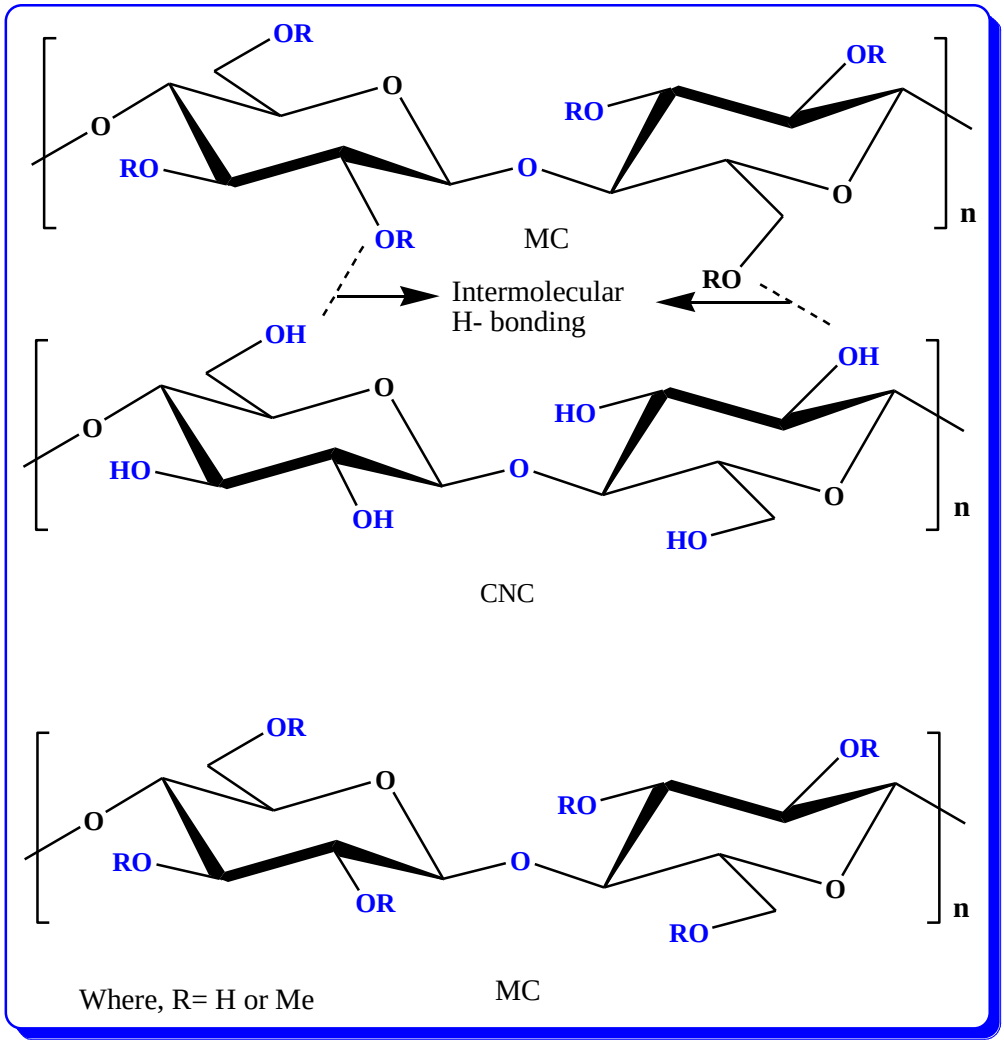

Figure 1. Path of interaction between MC and CNC in the nanocomposites through H-bonding (up) and chemical structure of MC (down).

Apart from reinforcing abilities, materials' biocompatibility is considered one of the most significant factors. There are so many inorganic resources (such as clay, graphene, mineral, etc.) for producing reinforcing fillers. These sources are non-renewable and expensive. In contrast, reinforcing agents from natural sources are more environment-friendly since plants isolate carbon by absorbing carbon dioxide and thus reduce greenhouse gas concentrations [31]. In this case, cellulose nanocrystals (CNC) used to develop bionanocomposites have attracted more and more attention in the field of nanotechnology. It has been widely demonstrated that incorporating CNC into biopolymers can result in bionanocomposite materials with high mechanical, optical, thermal, and barrier properties [32-39], which are the main properties required for packaging applications [40-45]. The adhesion properties and large-number functional groups in the CNC's surface and biopolymer matrices can be exploited to improve the interfacial interactions between CNC and biopolymer matrices [46-59].

In this study, methylcellulose and nanocellulose were used as matrix and filler, respectively, and amounts of methylcellulose (MC) were adjusted with various concentrations of crystalline nano cellulose (CNC) to form bio-composite films. This study has also characterized these newly formed bio-composite films with the help of ATR Fourier Transform Infrared (FTIR) spectroscopy. Thermo-chemical properties of the bio-composite films were determined by Thermo Gravimetric Analysis (TGA). The mechanical properties of the films were studied by controlled RH Dynamic Mechanical Analysis (DMA). The electrical conductivity of selected bio nanomaterial films was determined by controlled relative humidity dielectric analysis (DETA-RH). Optimizing CNC concentrations in newly prepared biocomposite films makes it possible to produce effective and environment-friendly materials like biodegradable packaging materials, automotive industries, and materials for agriculture and pharmaceuticals industries.

2. Materials and Methods

2.1. Materials.

Analytical grade chemicals such as Tylose were purchased from Shin-Etsu, UK. (MH 50 G4 Granules Ø < 500 µm), and CNC from Celluforce, Canada, were used to prepare nanocomposite films without further purification.

2.2. Nanocomposite films preparation.

The aim was to prepare films of Tylose with varying concentrations of crystalline nanocellulose that would be suitable for testing, particularly by dynamic mechanical and dielectric analysis. Tylose MH 50 was selected at a concentration of 1.5% (w/w). A solution of nanocellulose (1%, w/w) was prepared and was added to Tylose in defined proportions.

2.2.1. Method-1 (batch-1).

To prepare Tylose MH 50 (1.5%, w/w) (Shin-Etsu, UK. MH 50 G4 Granules Ø < 500 µm), the calculated amount of distilled water was taken in beakers placed on a magnetic stirrer with heating. When the water temperature became 35 ˚C, sample powder (0.240 g of Tylose MH 50) was added very slowly. After stirring for 1 hour, solutions were kept for 30 minutes to settle. After keeping in a sonicator for 15 min, 1% (w/w) CNC solution was prepared. The calculated amount of CNC solution was added into Tylose MH 50 solution while stirring in a

magnetic stirrer, and the CNC solution was added to it in a dropwise manner. After 30 minutes of stirring, sonication for 15 min was performed. Finally, all solutions were poured into Petri dishes and dried in an oven at 40˚C for 24 hours.

2.2.2. Method-2 (Batch-2 and Batch-3).

Tylose MH 50 (1.5% , w/w) was prepared first. When the water temperature rose to 35°C, MC powder was added very slowly to the water, and the solution was stirred to prevent agglomeration. After stirring for 1 hr and 30 mins, a homogeneous solution was obtained and was kept for 30 minutes to settle. Ultrasonication was done for 15 minutes to remove air bubbles and further dispersion of the Tylose MH 50. For preparing Tylose MH 50/CNC composite films, 1% (w/w) of CNC solution was prepared following the above procedure. Different contents of CNC solution (5%, 10%,15% and 20%) were dropwise added into Tylose MH 50 solutions with stirring. After 30 mins, ultrasonication for each solution was done for 15 min. And the homogeneous solutions were poured into plastic Petri dishes. The water was evaporated at room temperature for three days, and the films obtained were dried in an oven for 48 hours at 40°C.

2.3. ATR- FTIR characterization.

The FTIR spectra of the films were recorded in the region of 4000 cm^{-1} to 400 cm^{-1} by a PERKIN ELMER System 2000 FT-IR instrument with the SENSIR DuraScope accessory. This technique was used to analyze structural changes in the nanocomposite films. The spectra were analyzed by using Grams software. Films were stored at room temperature. FTIR analysis of Tylose MH 50 with different CNC concentrations was performed for each batch and compared to evaluate the effects of CNC filling in MC films based on the intensity and shift of vibrational bands.

2.4. Thermogravimetric analysis (TGA).

A Shimadzu TGA-50 was used to determine the thermal stability of the dried composite films. A small portion of the dried composite film was cut and placed in a Pt crucible and heated to 800°C at a rate of 10°C /min in purge gas (oxygen) at a flow rate of 60 ml min^{-1}.

2.5. Dynamic mechanical analysis of composite films.

The Dynamic Mechanical analysis with a humidity controller (Tritec 2000 Technology) was conducted at 1 Hz at 20% RH and 25°C. The dried films were measured in tension at a single frequency (1 Hz) and strain (0.1%). The dynamic load was applied here, and the measurements were made over time. DMA was also performed with the static load. A force up to 6N was applied at 0.2N/min at 20%RH. Stress-strain curves were plotted, and Young's modulus values were calculated from the slope.

2.6. Controlled RH dielectric analysis (DETA-RH).

A dielectric analyzer with a humidity controller (Lacerta Technology DS6000) was used for the measurement. The dried film sample was placed between two parallel plate electrodes. All samples were pre-dried for 24 hours before the measurement. After placing the sample in the instrument, RH decreased from 20% RH and remained there for about 20

minutes. Then RH was increased to 60% at a rate of 1% min. Once the RH reached the target, the sample remained at 60% RH for 15 minutes and then decreased from 1% min to 20% RH. The response of the sample was measured at five frequencies (0.3, 1.0, 3.0, 10.0, and 30.0 kHz) at a constant temperature of 25°C.

3. Results and Discussion

3.1. ATR- FTIR analysis.

The FTIR spectra of Tylose MH 50 (1.5%, w/w) composite film (control and with different CNC concentrations) were presented in Figure 2 and Figures S1-S4.

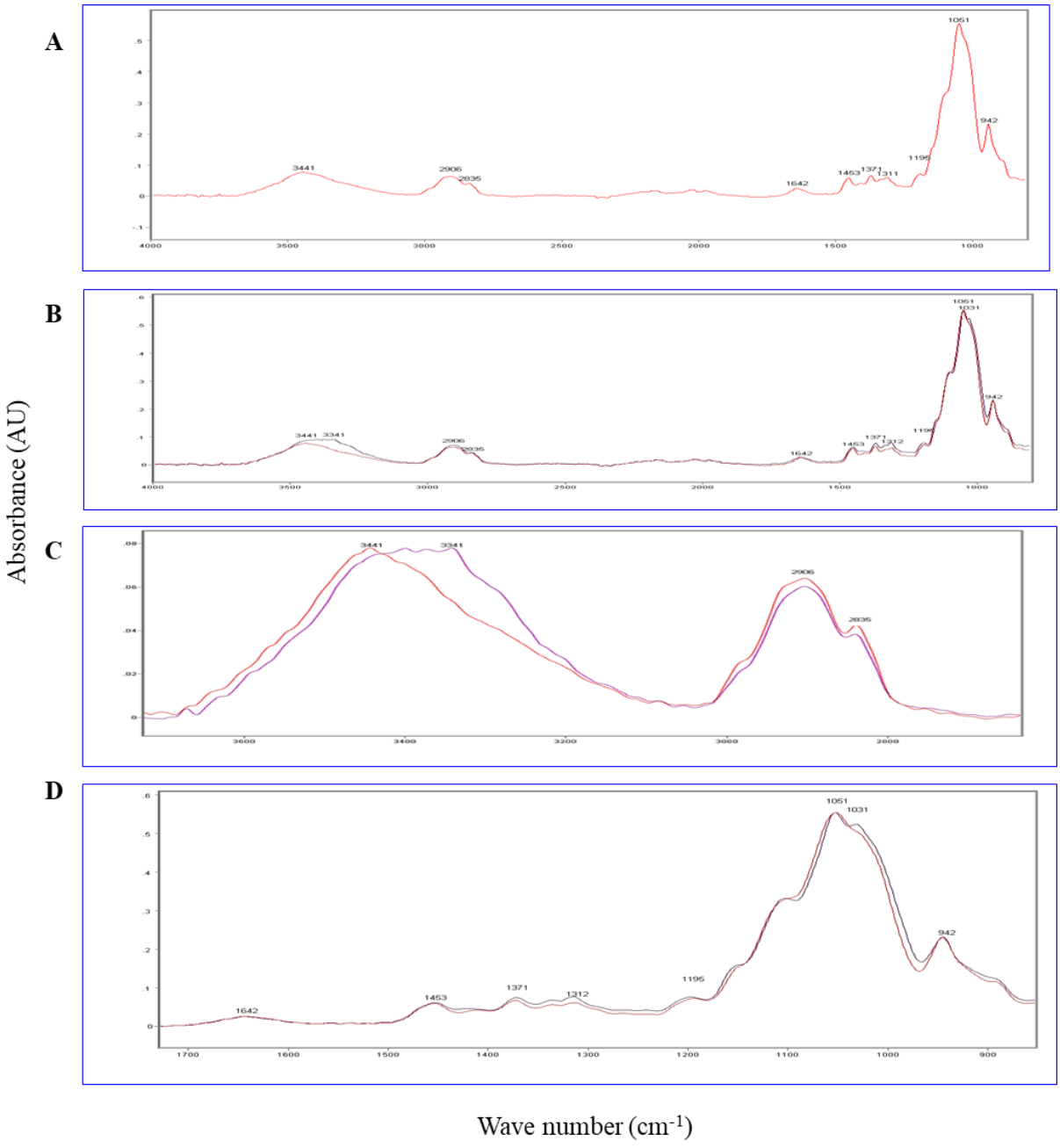

Figure 2. (**A**) FTIR spectra of Tylose MH 50 (1.5%, w/w) based film (control) of batch-1; (**B**) FTIR spectra of Tylose MH 50(1.5%, w/w) (red) and Tylose MH 50+15% CNC(w/w) (purple) composite films of batch 1; (**C**) Spectral region at 2700-3700 cm^{-1} of Tylose MH 50 (1.5%, w/w) (red) and Tylose+15%CNC (w/w) (purple) composite films of batch-1 and (**D**) FTIR spectra at the region 800-1800 cm^{-1} of Tylose MH 50 (1.5%, w/w) (red) and Tylose MH 50+15% CNC (w/w) (purple) composite films of batch-1.

In FTIR spectra, absorption peaks of 1.5% Tylose MH 50 at 3441 cm^{-1} and 2835-2906 cm^{-1} indicated stretching vibrations of OH and symmetric and asymmetric C-H vibrations, whereas peaks at 1642 cm^{-1} corresponded to OH bending of absorbed water (Figure 2A). The bending vibration of OH of absorbed water was difficult to extract due to the cellulose-water interaction. These peaks are shown to be MC peaks where OH stretching vibration was in the range of 3200-3600 cm^{-1}, symmetric and asymmetric stretching vibration of C-H were at 2835 -2980 cm^{-1}, and OH bending vibration of water was in 1600-1800 cm^{-1} [60-65]. Other peaks had been observed in the 1453 cm^{-1} due to CH_3 deformation in cellulose. Peaks at 1371 cm^{-1}, 1311 cm^{-1}, and 1195 cm^{-1} represented C-H bending in-plane and 1051 cm^{-1} corresponded to C-O groups. These peaks are shown to be the cellulose peaks if there are -CH_3 bending vibration at 1460 cm^{-1} ,CH bending at 1374 cm^{-1},1315 cm^{-1}, 1195 cm^{-1} and CO stretching at 1058 cm^{-1} [17, 35, 66]. The peak at 942 cm^{-1} observed in the Tylose MH 50 composites film control film could be associated with C-H monosubstituted out of plane bending for C-H. There was some difference observed in IR spectra due to the incorporation of CNC into Tylose MH 50 films (Figure 2B). Tylose MH 50 +15% CNC (w/w) films showed a shift in the absorption peaks for OH stretching vibration to the lower value (down from 3441 to 3341 cm^{-1}) (Figures 2B and 2C), which could be due to the interaction of hydroxyl groups of CNCs with OH groups of hydrophilic Tylose MH 50 polymer. This shift in peaks, from 3410 to a lower value of 3330 cm^{-1} was observed due to the incorporation of CNC into MC films [52]. An intense peak appeared at 1031 cm^{-1} with the incorporation of CNC into Tylose MH 50 film, which is assigned to CO stretching (carbonyl groups) (Figure 2D). The lower absorption from 1051 cm^{-1} to 1031 cm^{-1} happened due to the extended time of sonication [52, 64]. These spectra were developed by carefully drying the films for 3 days in the air and 24 hours in an oven at 40°C.

3.2. Thermogravimetric analysis (TGA).

Figure 3 represents the TGA and DTGA curves of crystalline nanocellulose type 1 (powder). TGA curves showed that major weight loss occurs between 200-400°C, followed by a much smaller weight loss between 450-600°C.

Table 1. Results of calculated weight loss (%) for selected temperature intervals with onset temperatures of degradation of composites films from batch-1.

Sample	Weight loss (%)		Onset Temperature of degradation (°C)	1st derivative (Temperature° C)
	200-400°C	450-600°C		
Crystalline nanocellulose type 1 (powder)	74.1	5.0	298	309

DTG curves showed the rate of mass change with temperature, the magnitude of peak width at half height provides information on this; the larger the value and the broader the peak, the slower the rate of degradation. The onset temperature of degradation of the first process in crystalline nanocellulose type 1 (powder) occurred at 298°C. Table 1 shows the result obtained from these curves. The magenta-colored DTG curve shown in Figure 3A has a narrower peak width. This narrower peak indicated that the rate of degradation was higher. The obtained TGA and DTGA curves (Figure 3B) for 1.5% Tylose MH 50 composite film of batch-1 indicate that major weight loss occurred between 200-400°C following a much smaller weight loss between 450-600 °C. DTG curves showed the rate of mass change with temperature, whereas the magnitude of peak width at half height provided information on this: Larger values and broader peaks showed a slower rate of degradation.

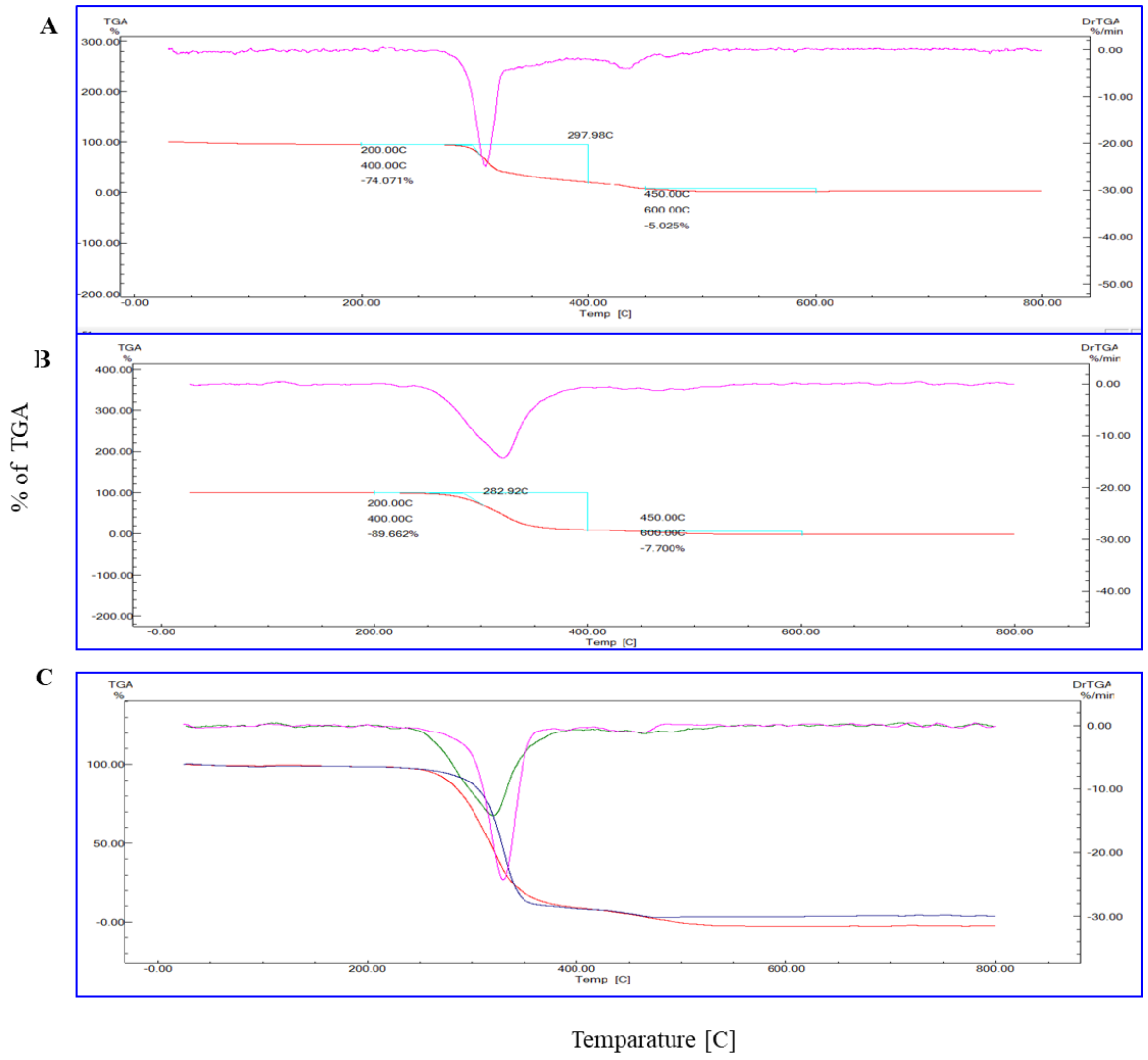

Figure 3. (A) TGA curves of crystalline nanocellulose type 1. **(B)** TGA (red) and DTGA (magenta) curves of 1.5% Tylose MH 50 composite film of batch-1. (**C**) TGA curves of 1.5% Tylose MH 50 (red), Tylose MH 50 +15% CNC (blue), DTGA curves of 1.5% Tylose MH 50 (green) and Tylose MH 50 +15% CNC (magenta).

The onset temperature of degradation of the first process in Tylose MH 50 (1.5%, w/w) film occurred at 283°C. With the incorporation of CNC into Tylose MH 50 film, the onset temperature of degradation was increased from 283°C to 308 °C (Figure 3B). Table 2 shows the results obtained from these curves.

Table 2. Results of calculated weight loss (%) for selected temperature intervals are shown together with an onset temperature of composites films batch-1.

Sample	Weight loss (%)		Onset Temperature of degradation (°C)	ΔT	1st derivative (Temperature° C)
	200-400°C	450-600°C			
Tylose MH50 (1.5%) (w/w)	89.7	7.70	283		320
Tylose MH50+15% CNC (w/w)	90.1	1.82	308	25.0	330

The magenta-colored DTG curve (Tylose MH 50+ 15% CNC) shown in Figure 3C had a narrower peak width at half height than that DTG curve for Tylose. The addition of crystalline CNC made the composite more crystalline resulting in a narrower peak in DTG.

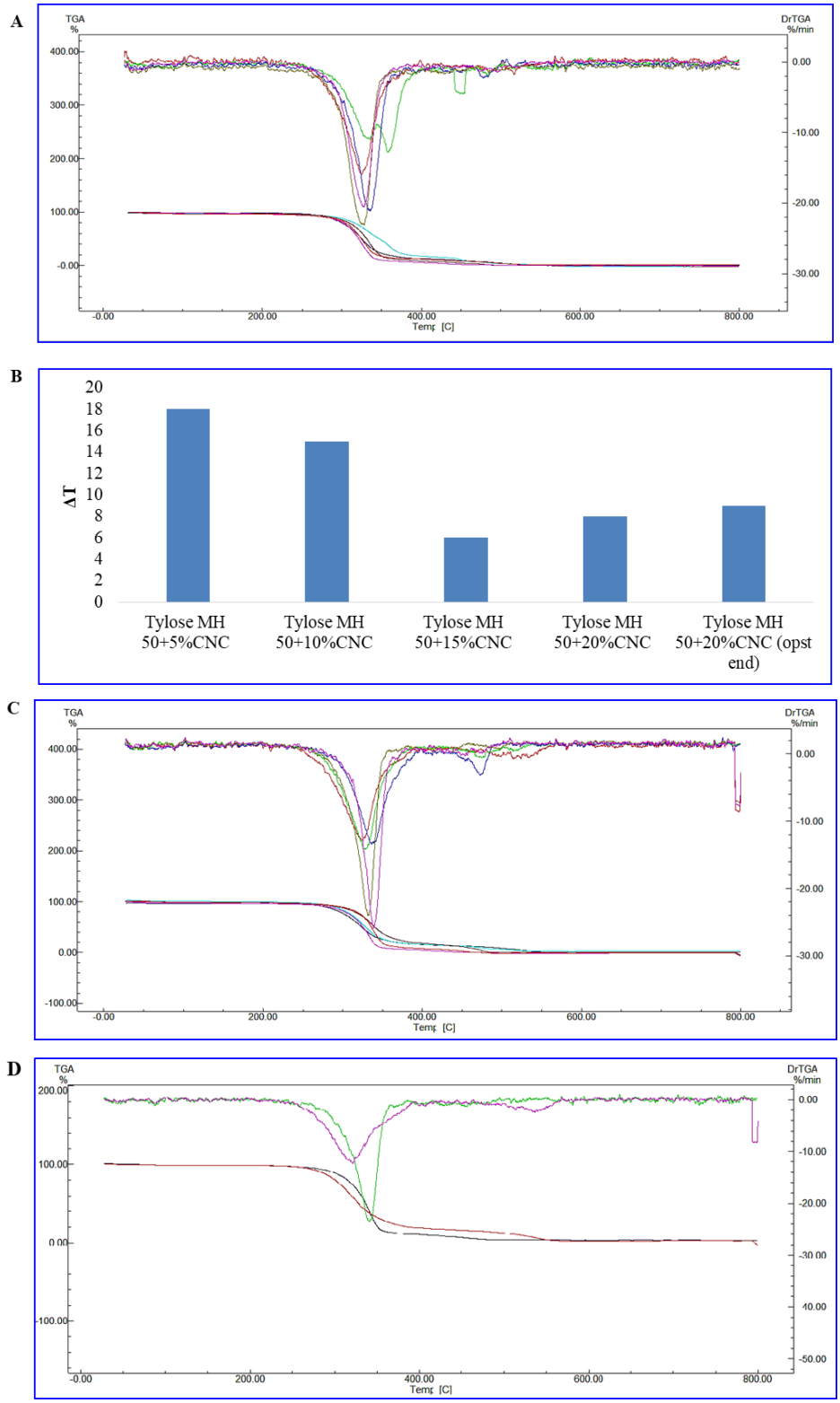

Figure 4. (**A**) TGA curves of 1.5% Tylose MH 50 (blue), Tylose MH 50 +5%CNC (cyan), Tylose MH 50+10% CNC (dark red), Tylose MH 50+15%CNC (magenta) and Tylose MH 50+20% CNC (red) films. DTGA curves of 1.5% Tylose MH 50 (red) and Tylose MH 50 +5% CNC (green), Tylose MH 50+10% CNC (blue), Tylose MH 50+15%CNC (brown) and Tylose MH 50+20% CNC (magenta) films of batch-2. (**B**) ΔT values of Tylose with CNC composites films of batch-2. (**C**) TGA curves of 1.5% Tylose MH 50 (blue) and Tylose MH 50+5%CNC (cyan), Tylose MH 50+10%CNC (dark red), Tylose MH 50+15%CNC (magenta) and Tylose MH 50+20% CNC (red) films. DTGA curves of 1.5% Tylose MH 50 (red), Tylose MH 50 +5% CNC (green),Tylose MH 50+10% CNC (blue), Tylose MH 50+15% CNC (brown) and Tylose MH 50+20% CNC (magenta) films of batch-3. (**D**) TGA curves of 1.5% Tylose MH 50 (red) and Tylose MH 50 +15% CNC (blue) and DTGA curves of 1.5% Tylose MH 50 (magenta) and Tylose MH 50 +15% CNC (green) composite films of batches 2 and 3.

That narrower peak also indicated a higher rate of degradation. DTG curves showed the maximum decomposition temperature at each stage of thermal degradation. From the first derivative curve, it is seen that the weight loss occurred very quickly for Tylose MH 50 with 15% CNC film, whereas the weight loss occurred slowly for Tylose MH 50 film. The first derivative peak (°C) also showed more thermal stability of Tylose MH 50+15% CNC than 1.5% Tylose MH 50 film.

TGA and DTGA curves of 1.5% Tylose MH 50 composites film batch-2 indicated that the major weight loss occurred between 200-400°C, followed by a much smaller weight loss between 450-600°C. The onset temperature of degradation of the first process in 1.5% Tylose MH 50 film occurred at 299°C. With the incorporation of CNC (5%,10%,15%,20%) into Tylose MH 50 film, the onset temperature of degradation increased from 299°C to 317°C, 314°C, 305°C, and 307°C, respectively, which means the film with 5% CNC was more thermally stable than that of neat Tylose MH 50 film and Tylose with CNC films (10%,15%, 20%) (Figure 4A). The results obtained from these curves are presented in Table 3. The green-colored DTG curve (Tylose MH 50+ 5% CNC) in Figure 4A had a broader peak width than the DTG curve for Tylose MH 50 and other Tylose +CNC composite films. The broader peak indicated that the rate of degradation is slower. The effect of adding crystalline CNC makes the composite more crystalline, with the result that DTG is a narrower peak. The narrower peak also indicates that the rate of degradation is higher. The brown-colored DTG curve (Tylose MH 50+15% CNC) has a narrower peak than neat Tylose MH 50 film and other nanocomposites films showing a higher rate of degradation with more crystallinity. It was expected that with the increase of CNC in composite films, the stability would be increased, but there was a variation in stability for all nanocomposites films. DTG curves showed the maximum decomposition temperature at each stage of thermal degradation. The first derivative peak (°C) also showed more thermal stability of Tylose MH 50+5%CNC nanocomposite films than neat Tylose MH 50 film and other nanocomposite films (10%, 15%, and 20%) (Figure 4A). The ΔT values (difference in onset temperature of degradation of nanocomposite films with respect to control film) of different composite films were shown in Figure 4B. From the ΔT (Difference of onset temperatures between two samples) values, it is seen that Tylose MH 50+5%CNC film was more stable than other nanocomposite films.

TGA and DTGA curves of 1.5% Tylose MH 50 composites film from batch-3 indicated a major weight loss between 200-400°C and a very little weight loss between 450-600°C. The onset temperature of degradation of the first process in 1.5% Tylose MH 50 film occurred at 299°C. With the incorporation of CNC (5%, 10%, 15%, and 20%) into Tylose MH 50 film, the onset temperature of degradation increased from 299°C to 303°C, 314°C, 311°C, and 320°C, respectively which means the film with 20% CNC was thermally more stable than neat Tylose MH 50 film and Tylose with CNC films (5%, 10%, and 15%), shown in Figure 4C. The results obtained from these curves were also presented in Table 4. The magenta-colored DTG curve (Tylose MH 50+ 20% CNC) in Figure 4C had a narrower peak width at half height than the DTG curve for neat Tylose MH 50 and other nanocomposite films.

The effect of adding crystalline CNC made the composite more crystalline as a narrower peak became evident, which also indicated that the rate of degradation was higher. DTGA curves showed the maximum decomposition temperature at each stage of thermal degradation. The first derivative peak (°C) also showed more thermal stability of Tylose MH 50+20% CNC nanocomposite films than neat Tylose MH 50 film and other nanocomposite films (10%,15%, and 20%) (Figure 4C). The ΔT values diagram showing the difference in

onset temperature of degradation of nanocomposite films with respect to the control film S1 was also drawn for different composite films. The ΔT values showed that Tylose MH 50+20%CNC film was more stable than other nanocomposite films. This is contradictory to the results obtained from batch 2, where Tylose MH 50+5% CNC was more thermally stable. This could be due to the heterogeneity of films.

Table 3. Results of calculated weight loss (%) for selected temperature intervals are shown together with the onset temperature of degradation of composites films of batch-2.

Sample	Weight loss (%)		Onset Temperature of degradation (°C)	ΔT	1st derivative (Temperature° C)
	200-400°C	450-600°C			
Tylose MH50 (1.5%) (w/w)	85.2	9.67	299		324
Tylose MH50+5% CNC (w/w)	79.2	12.1	317	18.0	359
Tylose MH50+10% CNC (w/w)	88.9	5.37	314	15.0	334
Tylose MH50+15% CNC (w/w)	91.3	2.49	305	6.0	326
Tylose MH50+20% CNC (w/w) (S1)	84.0	7.23	307	8.0	327
Tylose MH50+20% CNC (w/w)(opstend) (S2)	87.3	2.7	308	9.0	317

TGA and DTGA curves of 1.5% Tylose MH 50 composite film of AB P15.4.17 [36, 37] showed that major weight loss occurred between 200-400°C, and very small weight loss occurred between 450-600°C. The onset temperature of degradation of the first process in 1.5% Tylose MH 50 film occurred at 301°C.

Table 4. Calculated weight loss (%) for selected temperature intervals with onset temperatures of degradation of composites films from batch-3.

Sample	Weight loss (%)		Onset Temperature of degradation (°C)	ΔT	1st derivative (Temperature° C)
	200-400°C	450-600°C			
Tylose MH50 (1.5%) (w/w) (S1)	82.0	12.0	299		324
Tylose MH50 (1.5%) (w/w) (t 0.050 mm) (S2)	77.2	13.7	302		329
Tylose MH50 (1.5%) (w/w) (0.037) (S1)	83.8	10.0	303		328
Tylose MH50+5% CNC (w/w) (S1)	83.9	10.0	303	4.0	328
Tylose MH50+5% CNC (w/w) (t 0.02 mm) (S2)	83.7	11.2	304	5.0	328
Tylose MH50+10% CNC (w/w)	78.8	10.9	314	15.0	336
Tylose MH50+15% CNC (w/w) (S1)	91.8	2.12	311	12.0	332
Tylose MH50+15% CNC (w/w) (opst end) (S2)	90.9	0.383	313	15.0	325
Tylose MH50+20% CNC (w/w) (S1)	90.9	4.04	320	21.0	339
Tylose MH50+20% CNC (w/w) (S2)	85.2	5.69	319	20.0	336

With the incorporation of CNC into Tylose MH 50 film, the onset temperature of degradation increased from 301°C to 311°C. Table 5 shows the result obtained from these curves. The magenta-colored DTG curve for Tylose MH 50+ 15% CNC had a narrower peak width than the DTG curve for Tylose only. From the first derivative curve, it is seen that the weight loss occurred very quickly for Tylose MH 50 with 15% CNC film, whereas the weight loss was comparatively slower for Tylose MH 50 film. The first derivative peak also showed more thermal stability of Tylose MH 50+15% CNC than 1.5% Tylose MH 50 film. The first derivative peak also showed more thermal stability of Tylose MH 50+15% CNC film than 1.5% Tylose MH 50 film.

Table 5. Calculated weight loss (%) for selected temperature intervals with onset temperatures of degradation of composites films of AB P15.4.17.

Sample	Weight loss (%)		Onset Temperature of degradation (°C)	ΔT	1st derivative (Temperature° C)
	200-400°C	450-600°C			
Tylose MH50 (1.5%) (w/w)	82.3	11.7	301		326
Tylose MH50+15% CNC (w/w)	83.9	8.7	311	10.0	335

Similar to AB P15.4.17, TGA and DTGA curves of 1.5% Tylose MH 50 composite film of AB P24.7.17 [67, 68] showed a major weight loss between 200-400°C and minor weight loss between 450-600°C. The onset temperature of degradation occurred at 293°C. With the incorporation of CNC into Tylose MH 50 film, the onset temperature of degradation increased from 293°C to 310°C (Figure 4D). Results obtained from these curves are presented in Table 6. The green-colored DTG curve (Tylose MH 50+ 15% CNC) in Figure 4D also had a narrower peak width at half height than the DTG curve for Tylose only. Other results were also in line with AB P15.4.17.

Table 6. Calculated weight loss (%) for selected temperature intervals with an onset temperature of degradation of composites films of AB P24.7.17 & P25.7.17.

Sample	Weight loss (%)		Onset Temperature of degradation (°C)	ΔT	1st derivative (Temperature° C)
	200-400°C	450-600°C			
Tylose MH50 (1.5%) (w/w)	79.7	14.0	293		322
Tylose MH50+15% CNC (w/w)	88.1	3.66	310	17.0	341

3.3. Dynamics mechanical analysis of nanocomposite films Young's modulus (YM).

Young's modulus was determined for films of Tylose and Tylose with nanocellulose composite films (batch-1) prepared at 25°C under controlled relative humidity and set at 20%, and values were calculated from the ratio of stress to strain.

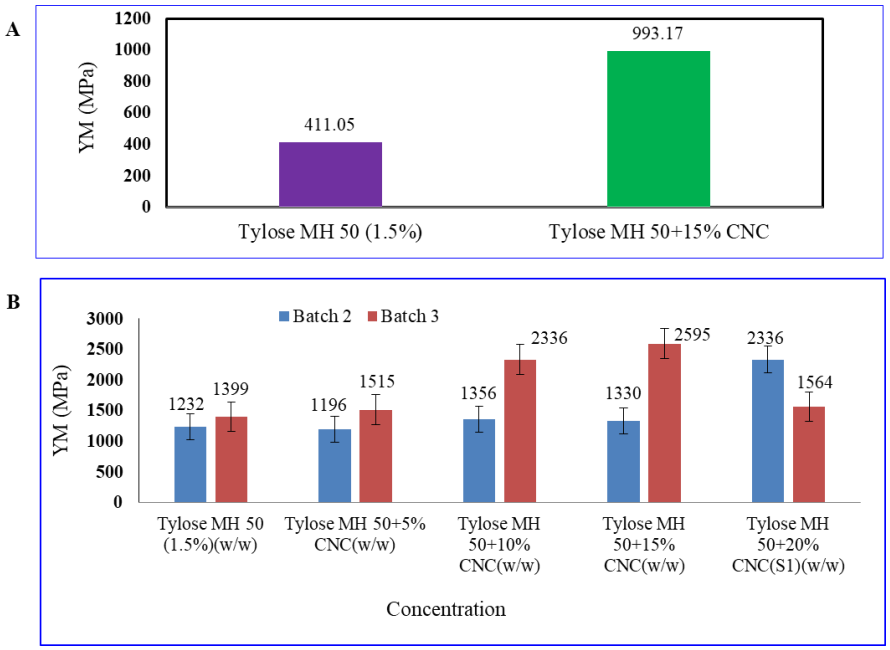

Figure 5. (**A**) Young's modulus measured at 20% RH and 25°C temperature for pre-dried 1.5% Tylose MH 50 and Tylose MH 50+15%CNC films of batch-1. (**B**) Young's modulus was measured at 20% RH and 25°C temperature for Tylose MH 50 (1.5%, w/w) and Tylose MH 50/CNC (w/w) composite films of batch-2 and batch-3.

The increase in Young's modulus (YM) (MPa) of the Tylose MH 50+15%CNC (w/w) film indicated increased stiffness of the film. As the concentration of CNC in the composite film increased, Young's modulus (MPa) increased by 142% (from 411.05 MPa to 993.17 MPa) (Figure 5A).

It was expected that with the incorporation of CNC to the Tyose MH 50, Young's modulus would be significantly enhanced due to the high aspect ratio of CNC and interfacial interaction due to hydrogen bonding between CNC and Tylose MH 50 matrix [69]. It was observed that there was an increase in Young's modulus (YM) for the incorporation of 10% to 20% CNC, resulting in increased stiffness of films under controlled relative humidity (RH) and controlled temperature at 25°C except for Tylose MH 50+5% CNC film, which was less stiff than 1.5% Tylose MH 50 film. However, the amount of fillers is an important factor in the fabrication of biocomposite films. The reinforcement started from 10% CNC incorporation to Tylose MH 50 matrix film in this batch. All the measurements were carried out at least three times for each sample on the same sample. Two samples from Tylose MH 50 +20% CNC films were measured to check the homogeneity of the sample (Figure 5B).

Young's modulus of Tylose MH 50 + 20% CNC (w/w) film was less than that of Tylose MH 50+15% CNC(w/w) film. But it was still greater than 1.5% Tylose MH 50 film indicating a less stiff film than Tylose with 15% CNC. The higher the value of Young's modulus, the higher the stiffness of films. Figure 5B indicated a significant difference in the stiffness of composite films of batch-2 and batch-3.

The calculated Young's modulus of Tylose MH 50 and Tylose MH 50/CNC composite films [67, 68] for AB P 15.4.17 are provided in Table 7 at 25°C temperature under controlled relative humidity (RH) and set at 20%. All the measurements were carried out at least three times for each sample on the same sample. Two samples from Tylose MH 50 (1.5%, w/w) films were measured to check the homogeneity of the sample. The present study also indicated the homogeneity of both samples (S1, S2) as there was no significant difference in their Young's modulus (MPa).

Table 7. Young's modulus value of Tylose MH 50 (1.5%, w/w, S1, S2) and Tylose MH 50+15%CNC(w/w) pre-dried composite films of AB P15.4.17.

Sample	Young's modulus (MPa)	STDEV
Tylose MH50 (1.5%, w/w, S1)	427.9	28.17
Tylose MH 50(1.5%, w/w, S2)	498.5	36.98
Tylose MH 50+15% (w/w) CNC	1626.0	129.5

3.4. Storage Modulus (SM), E′.

The measured dimensions of 1.5% Tylose MH 50 and Tylose MH 50+15% CNC dried films prepared for batch-1 are provided in Table 8. The storage modulus (MPa) of the Tylose MH 50+15% CNC nanocomposite film was higher than the storage modulus of neat 1.5% Tylose MH 50 film.

Table 8. Sample dimension and analysis of Tylose MH 50 (1.5%, w/w) and Tylose MH 50+15% CNC pre-dried composite films of batch-1.

Sample	Sample width (mm)	Sample thickness (mm)	Storage modulus,E′ (MPa)
Tylose MH 50 (1.5%, w/w)	5.683	0.041	707.6
Tylose MH 50+15% CNC (w/w)	5.410	0.032	1572

This increased storage modulus value indicates a strong reinforcement effect obtained with the incorporation of CNC. Therefore, higher storage modulus E' (MPa) means stiffer and more durable film. Figure 6A showed the storage modulus values of 1.5% Tylose MH 50 pre-dried composite films of batch-1with respect to time.

Table 9 provided the measured dimensions of 1.5% Tylose MH 50 and Tylose MH 50+15% CNC dried films [38, 39], prior to dynamic mechanical analysis at 25°C under controlled relative humidity and set at 20%. The storage modulus E′(MPa) of the Tylose MH 50+15% CNC nanocomposite film was higher than the storage modulus of neat 1.5% Tylose MH 50 film resulting in a stiffer and more durable film.

Table 9. Sample dimension and analysis of Tylose MH 50 (1.5%, w/w) and Tylose MH 50+15% CNC(w/w) pre-dried composite films of AB.

Sample	Sample width (mm)	Sample thickness (mm)	Storage modulus,E′ (MPa)
Tylose MH 50 (1.5%, w/w)	5.681	0.043	1049
Tylose MH 50+15% CNC (w/w)	5.650	0.033	1464

The measured dimensions of Tylose MH 50 (1.5%, w/w) and Tylose MH 50+15% CNC dried films for batches P24.7.17 & P25.7.17. The storage modulus, E′(MPa) of the Tylose MH 50+15% CNC dried nanocomposite film showed a greater value than that of 1.5% neat Tylose MH 50(1.5%, w/w) film (Figure 6B).

3.5. Effect of humidity cycles (EHC) on the properties of tylose MH 50 and tylose MH 50+15% CNC composite films.

The mechanical properties of Tylose MH 50 nanocomposite films were investigated based on three humidity cycles. The storage modulus measured at 25°C and relative humidity (20% & 60%) for 1.5%, Tylose MH 50 film after each successive humidity cycle is presented in Table 10. The decreased storage modulus at higher relative humidity (60% RH) was due to the hydrogen bonds created between chains in the Tylose MH 50 composite film by the absorption-desorption of water [70].

On the other hand, the Tylose MH 50+15% CNC composite films showed a higher storage modulus than the neat Tylose MH 50 film at 20% and 60% RH (Table 11). The humidification cycle increased the water concentration in the interface of the Tylose MH 50+15%CNC matrix (hydrogen bonds between the chains in Tylose MH 50), which was replaced by CNC, which formed CNC-Tylose MH 50 bonds, gave strength to the nanocomposite. The ΔE′ values (Figure 6C) show less difference in storage modulus with CNC incorporation between 20% and 60% RH in each cycle than the ΔE′ values of neat Tylose MH 50 film, which indicates the higher strength of Tylose MH 50+15%CNC composite films than the neat Tylose MH 50 film at 20% and 60% RH.

Table 10. The storage modulus measured at 25°C, and relative humidity 20% & 60% for Tylose MH 50(1.5%, w/w) pre-dried composite film of AB P24.7.17.

Relative humidity (% RH)	Storage Modulus, E′ (MPa)						Observation
	Time (min)	First cycle	Time (min)	Second cycle	Time (min)	Third cycle	
20	62.8	882.2	140.0	926.4	222.3	967.4	1
60	101.1	743.9	179.8	764.7	260.2	789.2	2

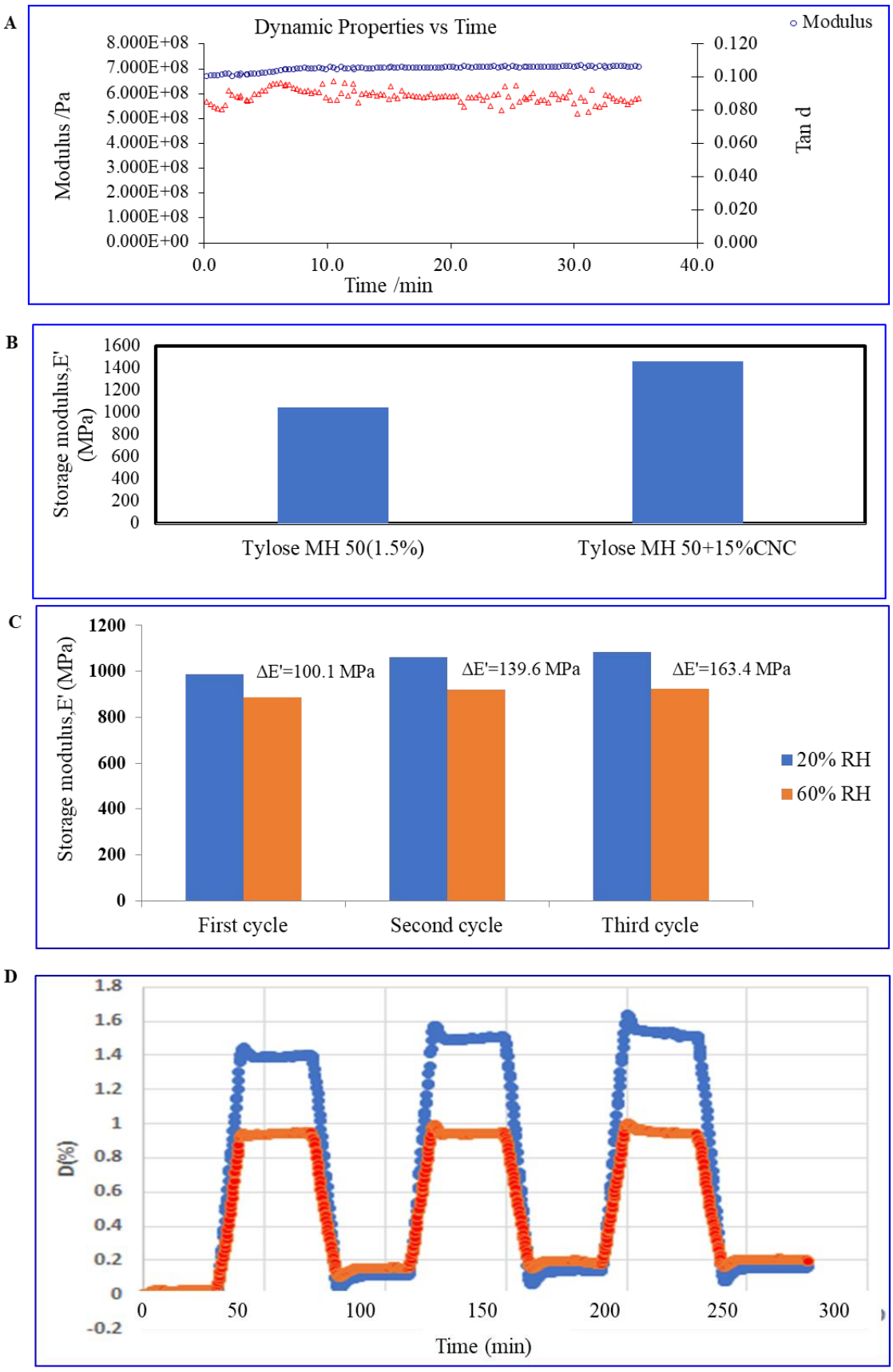

Figure 6. (A) The storage modulus for Tylose MH 50+15%CNC (w/w) pre-dried film of AB P25.7.17; (**B**) Storage modulus E′(MPa) of pre-dried Tylose MH 50(1.5%, w/w) (blue) and Tylose MH50+15%CNC(w/w) (red) films with respect to time(mins) of AB P24.7.17. (**C**) Storage modulus, E′(MPa) values of Tylose MH 50 (1.5%, w/w) and Tylose MH 50+15%CNC (w/w) pre -dried films of AB P24.7.17 & P25.7.17. (**D**) Displacement (%) of Tylose MH 50 (1.5%, w/w) pre-dried composite films of batch-1.

The displacement (%) of Tylose MH 50 (1.5%, w/w) and Tylose MH 50+15% CNC (w/w) composite films with respect to time (min) and relative humidity (%RH) is shown in Figure 6D. Displacement was zeroed so that the starting point for both the composite films was 30 mins before the first cycle. The reduction in displacement was seen for the Tylose MH 50+15% CNC composite films than Tylose MH 50 film without CNC, which indicated a stronger interaction between CNC-Tylose MH 50 film interfaces indicated the increased strength of nanocomposite film. The large displacement of Tylose MH 50 (control) films means more flexible hydrogen bonds between chains of Tylose MH 50 and between Tylose MH 50 with water molecules due to the humidification cycle as it increased water content in the composite film.

Table 11. The storage modulus measured at 25°C and relative humidity (20% & 60%) for Tylose MH 50 +15%CNC (w/w) pre-dried composite film of AB P25.7.17.

Relative humidity (% RH)	Storage Modulus, E′ (MPa)						Observation
	Time (min)	First cycle	Time (min)	Second cycle	Time (min)	Third cycle	
20	26.9	986.6	106.5	1061.0	186.0	1086.0	1
60	63.4	886.5	142.8	921.6	224.4	224.4	2

3.6. DETA-RH: nanocellulose concentration.

The values for complex permittivity ε*, relative permittivity, and dielectric loss at 60% RH for Tylose MH 50 (1.5%, w/w) film without CNC of AB P15.4.17 were presented in Table 12. The sample was kept at 60% RH for 15 minutes, and then RH was decreased to 1% min for Tylose MH 50 (1.5%, w/w) film. As the RH increases, the permittivity of the dried films increases gradually. There is a gradual increase in relative permittivity when the RH is held at 60%. When the RH decreases from 60%, the permittivity also decreases. The observed increase in permittivity occurs as water is absorbed. Water has a higher value of relative permittivity (dielectric constant) than film.

The plot of dielectric loss Vs. 1/ω was shown in Figure 7A. The measured values of slopes showed the conductivity of dried films at 60% RH. The calculated slope had a value of 0.5078. The electric conductivity calculated at 60% RH was $\sigma_{conductivity}$=slope× ε_0 where ε_0=8.85 pFm^{-1}. Therefore, the electrical conductivity for Tylose MH 50 (1.5%, w/w) film was 8.85 ×0.5078=4.49 Sm^{-1}.

Table 12. Measured values for permittivity, dielectric loss, complex permittivity ε*, at the end of the plateau at 60% RH for Tylose MH 50(1.5%, w/w) pre-dried film without CNC.

Time	° C	Frequency	Capacitance	Tan Delta	ε'	ε''	ε*	Ionic Conductivity	Humidity	1/ω	ε''
Tylose MH 50 (1.5%, w/w)											
5392	24.6	0.3	52.507	0.132	1.586	0.209	1.600	3.49 E-09	60.1	0.531	0.209
5407	24.6	1	48.838	0.083	1.475	0.122	1.481	6.79 E-09	60.1	0.159	0.122
5422	24.6	3	46.823	0.053	1.415	0.075	1.417	1.25E-08	60.0	0.053	0.075
5437	24.6	10	45.618	0.034	1.378	0.047	1.379	2.6E-08	60.1	0.016	0.047
5453	24.6	30	45.303	0.023	1.369	0.032	1.369	5.29E-08	60.1	0.005	0.032

The values for complex permittivity ε*, relative permittivity, and dielectric loss at 60% RH for Tylose MH 50(1.5%, w/w) film with CNC of AB P15.4.17 [36, 37] were presented in Table 13. The values of electrical conductivity in Table 14 are for the Tylose MH 50(1.5%, w/w) film without CNC (Figure 7A) and Tylose MH 50 with 15% CNC (w/w) film (Figure 7B). The value of slope and conductivity in the Tylose MH 50 (1.5%, w/w) film without CNC

is low, which indicates the film was less hydrophilic in comparison to Tylose MH 50 with 15% CNC (w/w) (Figure 7C) as CNC is more hygroscopic, i.e., absorbed more water.

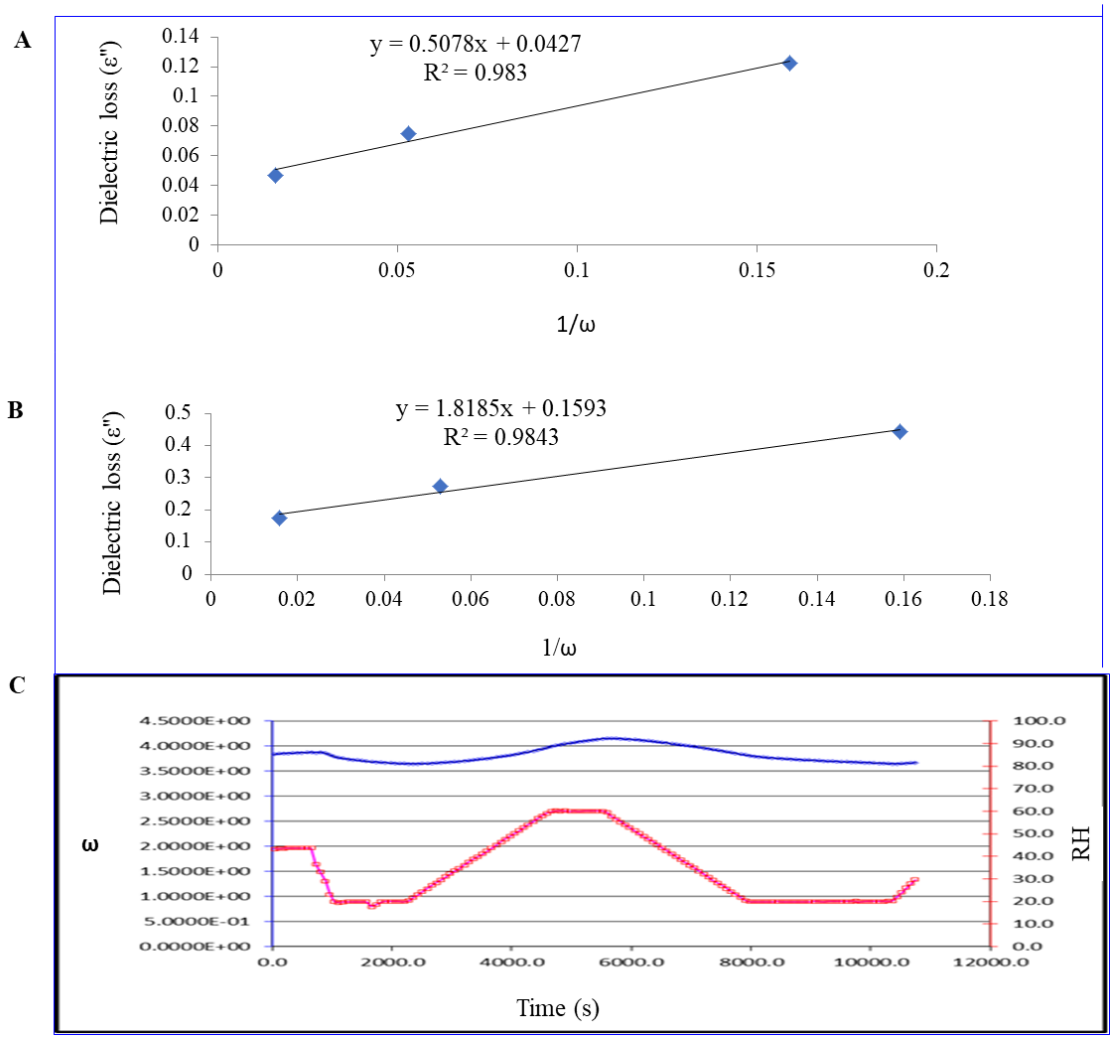

Figure 7. (**A**) Plot of dielectric loss Vs 1/ω for pre-dried Tylose MH 50(1.5%, w/w) film without CNC. (**B**) Plot of dielectric loss Vs 1/ω for pre-dried Tylose MH 50+15% CNC (w/w) composite film of AB P15.4.17. (**C**) Pre-dried Tylose MH 50+15%CNC(w/w) film: Variation of permittivity ε′(blue) with increasing relative humidity (RH) of 1% min (red) versus time (secs) of AB P15.4.17.

Table 13. Measured values for permittivity, dielectric loss, and complex permittivity ε*, at the end of the plateau at 60% RH for pre-dried Tylose MH 50 +15% CNC(w/w) composite film of AB 15.4.17.

Time	°C	Frequency	Capacitance	Tan Delta	ε'	ε''	ε*	Ionic Conductivity	Humidity	1/ω	ε''
Tylose MH 50+15% CNC (w/w)											
5496	24.8	0.3	77.638	0.168	4.579	0.768	4.644	1.28E-08	60.1	0.531	0.768
5511	24.8	1	70.309	0.107	4.147	0.444	4.171	2.47E-08	60.1	0.159	0.444
5526	24.7	3	66.470	0.070	3.921	0.275	3.931	4.58E-08	59.7	0.053	0.275
5542	24.7	10	64.095	0.046	3.781	0.175	3.785	9.68E-08	59.8	0.016	0.174
5558	24.7	30	63.194	0.033	3.727	0.123	3.730	2.05E-07	60.0	0.005	0.123

Table 14. Gradient and electrical conductivity (Sm^{-1}) of Tylose MH 50 (1.5%, w/w) without CNC and Tylose MH 50+15%CNC(w/w) pre-dried composite films of AB P15.4.17.

Figure	Tylose MH 50+ %CNC (w/w) film	Gradient	Electrical conductivity(Sm-1)
8	0%	0.51	4.49
9	15%	1.82	16.1

4. Conclusions

Bio-composite films were prepared using methylcellulose (MC) with various concentrations of CNC, and their characterizations were determined successfully by ATR FTIR, TGA, DMA-RH, and DETA-RH methods. FTIR of all batches of samples showed a similar sort of molecular arrangement. With the addition of CNC into the Tylose MH 50 (1.5%, w/w) solution, optimal characteristics were provided to increase thermal stability and film strength. TGA study of Tylose MH 50+CNC nanocomposite films showed a significant difference in thermal stability. An increase in Young's modulus (YM) for all samples indicated the presence of CNC in the Tylose MH 50 matrix, pointing to the stiffness of composites films. An increase in storage modulus (E) at 1 Hz evidenced the reinforcement of composite films. Another important property of nanocellulose is their behavior toward moisture absorption, which provides information on their hydrophilic nature. Evaluation of the dielectric analysis allows for optimization of this hydrophilic nature based on conductivity and moisture absorbance. Further investigations, including mixing time controlled drying temperatures, using higher CNC concentrations, and observing their effects on Tylose MH 50 composite films characterization, will help to understand bionanocomposite films' mechanical and thermal properties. Long mixing time, doubling the volume by adjusting the weight for the same coverage, or using smaller Petri dishes can be suggested to analyze the future thermomechanical and dielectric properties of bionanocomposite films.

Funding

This research received no external funding.

Acknowledgments

The authors thank Dr. Alexandra Bridarolli, analytical chemistry program at the Birkbeck, the University of London, for supporting this work.

Conflicts of Interest

The authors declare that there are no conflicts of interest.

References

1. Aaliya, B.; Sunooj, K.V.; Lackner, M. Biopolymer composites: a review. *International Journal of Biobased Plastics* **2021**, *3*, 40-84, https://doi.org/10.1080/24759651.2021.1881214.
2. Tang, X.Z.; Kumar, P.; Alavi, S.; Sandeep, K.P. Recent advances in biopolymers and biopolymer-based nanocomposites for food packaging materials. *Critical Reviews in Food Science and Nutrition* **2012**, *52*, 426–442, https://doi.org/10.1080/10408398.2010.500508.
3. Zeng, Q.; Xiao, N.; Zhang, X.; Luo, W.; Xiao, G.; Zhai, W.; Zhong, L.; Lan, B. Preparation and Characterization of Chinese Leek Extract Incorporated Cellulose Composite Films. *Progress in Polymer Science* **2021**, *2*, 731749, https://dx.doi.org/10.3389%2Ffbioe.2021.731749.
4. Atta, O.M.; Manan, S.; Ahmed, A.A.Q.; Awad, M.F.; Ul-Islam, M.; Subhan, F.; Ullah, M.W.; Yang, G. Development and Characterization of Yeast-Incorporated Antimicrobial Cellulose Biofilms for Edible Food Packaging Application. *Polymers* **2021**, *13*, 2310, https://doi.org/10.3390/polym13142310.
5. Baranenko, D.; Boulkrane, M.S.; Borisova, I.; Astafyeva, B.; Lu, W.; El-Aty, A.M.A. Translocation of pathalates from food packing materials into minced beef. *Frontiers in Nutrition* **2022**, *8*, 813553, https://doi.org/10.3389/fnut.2021.813553.

6. Li, Y.; Chen, Y.; Wu, Q.; Huang, J.; Zhao, Y.; Li, Q.; Wang, S. Improved hydrophobic, UV barrier and antibacterial properties of multifunctional PVA nanocomposite films reinforced with modified lignin contained cellulose nanofibers. *Polymers* **2022**, *14*, 1705, https://doi.org/10.3390/polym14091705.
7. Trifol, J.; Moriana, R. Barrier packaging solutions from residual biomass: Synergetic properties of CNF and LCNF in films. *Industrial Crops and Products* **2022**, *177*, 114493, https://doi.org/10.1016/j.indcrop.2021.114493.
8. Faruk, O.; Bledzki, A.K.; Fink, H.P.; Sain, M. Biocomposites reinforced with natural fibers: 2000–2010. *Progress in Polymer Science* **2012**, *37*, 1552–1596, https://doi.org/10.1016/j.progpolymsci.2012.04.003.
9. Jawaid, M.; Abdul Khalil, H.P.S. Cellulosic/synthetic fibre reinforced polymer hybrid composites: A review. *Carbohydrate Polymers* **2011**, *86*, 1–18, https://doi.org/10.1016/j.carbpol.2011.04.043.
10. John, M.J.; Thomas, S. Biofibres and biocomposites. *Carbohydrate Polymers* **2008**, *71*, 343–364, https://doi.org/10.1016/j.carbpol.2007.05.040.
11. Khan, A.; Huq, T.; Khan, R.A.; Riedl, B.; Lacroix, M. Nanocellulose-based composites and bioactive agents for food packaging. *Critical Reviews in Food Science and Nutrition* **2014**, *54*, 163–174, https://doi.org/10.1080/10408398.2011.578765.
12. Siqueira, G.; Bras, J.; Dufresene, A. Cellulosic bionanocomposites: A review of preparation properties and applications. *Polymers* **2010**, *2*, 728–765, https://doi.org/10.3390/polym2040728.
13. Narasagoudr, S.S.; Hegde, V.G.; Vanjeri, V.N.; Chougale, R.B.; Masti, S.P. Ethyl vanillin incorporated chitosan/poly(vinyl alcohol) active films for food packaging applications. *Critical Reviews in Food Science and Nutrition* **2020**, *236*, 116049, https://doi.org/10.1016/j.carbpol.2020.116049.
14. Srikhao, N.; Kasemsiri, P.; Ounkaew, A.; Lorwanishpaisarn, N.; Okhawilai, M.; Pongsa, U.; Hiziroglu, S.; Chindaprasirt, P. Bioactive nanocomposite film based on cassava starch/polyvinyl alcohol containing green synthesized silver nanoparticles. *Journal of Polymer and the Environment* **2020**, *29*, 672-684, https://doi.org/10.1007/s10924-020-01909-2.
15. Pinto, L.; Bonifacio, M.A.; De Giglio, E.; Santovito, E.; Cometa, S.; Bevilacqua, A.; Baruzzi, F. Biopolymer hybrid materials: development, characterization, and food packaging applications. *Food Packaging and Shelf Life* **2021**, *28*, 100676, https://doi.org/10.1016/j.fpsl.2021.100676.
16. Narasagoudr, S.S.; Hegde, V.G.; Chougale, R.B.; Masti, S.P.; Vootla, S.; Malabadi, R.B. Physico-chemical and functional properties of rutin induced chitosan/poly (vinyl alcohol) bioactive films for food packaging applications. *Food Hydrocolloids* **2020**, *109*, 106096, https://doi.org/10.1016/j.foodhyd.2020.106096.
17. Sánchez-López, A.L.; Perfecto-Avalos, Y.; Sanchez-Martinez, A.; Ceballos-Sanchez, O.; Sepulveda-Villegas, M.; Rincón-Enríquez, G.; Rodriguez-Gonzalez, V.; Garcia-Varela, R.; Lozano, L.M.; Navarro-Lopez, D.E.; Sanchez-Ante, G.; Corona-Romero, K.; Lopez-Mena, E.R. Influence of erbium doping on zinc oxide nanoparticles: structural, optical and antimicrobial activity. *Applied Surface Science* **2022**, *575*, 151764, https://doi.org/10.1016/j.apsusc.2021.151764.
18. Boonsiriwit, A.; Itkor, P.; Sirieawphikul, C.; Lee, Y.S. Characterization of Natural Anthocyanin Indicator Based on Cellulose Bio-Composite Film for Monitoring the Freshness of Chicken Tenderloin. *Molecules* **2022**, *27*, 2752-2766, https://doi.org/10.3390/molecules27092752.
19. Yu, Z.; Tan, Y.; Luo, S.; Zhou, J.; Xu, T.; Zou, J.; Ke, L.; Yu, J.; Zhang, S.; Zhou, J.; Rao, P.; Li, J. Food nanoparticles from rice vinegar: isolation, characterization, and antioxidant activities. *Npj Science of Food* **2022**, *6*, 1, https://doi.org/10.1038/s41538-021-00118-y.
20. Kamarudin, S.H.; Rayung, M.; Abu, F.; Ahmad, S.; Fadil, F.; Karim, A.A.; Norizan, M.N.; Sarifuddin, N.; Mat Desa, M.S.Z.; Mohd Basri, M.S.; Samsudin, H.; Abdullah, L.C. A review on antimicrobial packaging from biodegradable polymer composites. *Polymers* **2022**, *14*, 174, https://doi.org/10.3390/polym14010174.
21. Pirsa, S.; Sani, I. K.; Mirtalebi, S.S. Nano-biocomposite based color sensors: investigation of structure, function, and applications in intelligent food packaging. *Food Packaging and Shelf Life* **2022**, *31*, 100789, https://doi.org/10.1016/j.fpsl.2021.100789.
22. Sultana, A.; Kathuria, A.; Gaikwad, K.K. Metal–organic frameworks for active food packaging. A review. *Environmental Chemistry Letters* **2022**, *20*, 1479-1495, https://doi.org/10.1007/s10311-022-01387-z.
23. Hosseini, H.; Zirakjou, A.; McClements, D.J.; Goodarzi, V.; Chen, W.H. Removal of methylene blue from wastewater using ternary nanocomposite aerogel systems: carboxymethyl cellulose grafted by polyacrylic acid and decorated with graphene oxide. *Journal of Hazardous Materials* **2022**, *421*, 126752, https://doi.org/10.1016/j.jhazmat.2021.126752.

24. Chua, K.Y.; Azzahari, A.D.; Abouloula, C.N.; Sonsudin, F.; Shahabudin, N.; Yahya, R. Cellulose-based polymer electrolyte derived from waste coconut husk: residual lignin as a natural plasticizer. *Journal of Polymer Research* **2020**, *27*, 115-124, https://doi.org/10.1007/s10965-020-02110-8.
25. Simona, J.; Dani, D.; Petr, S.; Marcela, N.; Jakub, T.; Bohuslava, T. Edible films from carrageenan/orange essential oil/trehalose—structure, optical properties, and antimicrobial activity. *Polymers* **2021**, *13*, 332-350, http://dx.doi.org/10.3390/polym13030332.
26. Yang, K.; Zhang, F.; Chen, Y.; Zhang, H.; Xiong, B.; Chen, H. Recent progress on carbon-based composites in multidimensional applications. *Composites Part A: Applied Science and Manufacturing* **2022**, *157*, 106906, https://doi.org/10.1016/j.compositesa.2022.106906.
27. Ghanbarzadeh, B.; Almasi, H.; Entezami, A.A. Physical properties of edible modified starch/carboxymethyl cellulose films. *Innovative Food Science and Emerging Technologies* **2010**, *11*, 697–702, https://doi.org/10.1016/j.ifset.2010.06.001.
28. Sionkowska, A. Current research on the blends of natural and synthetic polymers as new biomaterials: Review. *Progress in Polymer Science* **2011**, *36*, 1254–1276, https://doi.org/10.1016/j.progpolymsci.2011.05.003.
29. Mani, P.; Suresh, S. Vibrational spectra and naormal coordinate analysis of acetic acid cyclohexyl ester. *Rasayan Journal of Chemistry* **2009**, *2*, 307–311.
30. Liu, H.; Liu, D.; Yao, F.; Wu, Q. Fabrication and properties of transparent polymethylmethacrylate/cellulose nanocrystals composites. *Bioresource Technology* **2010**, *101*, 5685–5692, https://doi.org/10.1016/j.biortech.2010.02.045.
31. Karimi, S.; Tahir, P.M.; Karimi, A.; Dufresne, A.; Abdulkhani, A. Kenaf bast cellulosic fibers hierarchy: A comprehensive approach from micro to nano. *Carbohydrate Polymers* **2014**, *101*, 878–885, https://doi.org/10.1016/j.carbpol.2013.09.106.
32. Alves, J.S.; dos Reis, K.C.; Menezes, E.G.T.; Pereira, F.V.; Pereira, J. Effect of cellulose nanocrystals and gelatin in corn starch plasticized films. *Carbohydrate Polymers* **2015**, *115*, 215–222, https://doi.org/10.1016/j.carbpol.2014.08.057.
33. Samir, M.A.S.A.; Alloin, F.; Sanchez, J.Y.; Dufresne, A. Cellulose nanocrystals reinforced poly (oxyethylene). *Polymer* **2004**, *45*, 4149–4157, https://doi.org/10.1016/j.polymer.2004.03.094.
34. Chen, Y.; Liu, C.; Chang, P.R.; Cao, X.; Anderson, D.P. Bionanocomposites based on pea starch and cellulose nanowhiskers hydrolyzed from pea hull fibre: Effect of hydrolysis time. *Carbohydrate Polymers* **2009**, *76*, 607–615, https://doi.org/10.1016/j.carbpol.2008.11.030.
35. El Miri, N.; Abdelouahdi, K.; Zahouily, M.; Fihri, A.; Barakat, A.; Solhy, A.; Achaby, M.E. Bio-nanocomposite films based on cellulose nanocrystals filled polyvinyl alcohol/chitosan polymer blend. *Journal of Applied Polymer Science* **2015**, *132*, 42004, https://doi.org/10.1002/app.42004.
36. Fortunati, E.; Luzi, F.; Puglia, D.; Petrucci, R.; Kenny, J.M.; Torre, L. Processing of PLA nanocomposites with cellulose nanocrystals extracted from Posidoniaoceanica waste: Innovative reuse of coastal plant. *Industrial Crops and Products* **2015**, *67*, 439–447, https://doi.org/10.1016/j.indcrop.2015.01.075.
37. Fortunati, E.; Puglia, D.; Luzi, F.; Santulli, C.; Kenny, J.M.; Torre, L. Binary PVA bio-nanocomposites containing cellulose nanocrystals extracted from different natural sources: Part I. *Carbohydrate Polymers* **2013**, *97*, 825–836, https://doi.org/10.1016/j.carbpol.2013.03.075.
38. Kamal, M.R.; Khoshkava, V. Effect of cellulose nanocrystals (CNC) on rheological and mechanical properties and crystallization behavior of PLA/CNC nanocomposites. *Carbohydrate Polymers* **2015**, *123*, 105–114, https://doi.org/10.1016/j.carbpol.2015.01.012.
39. Mariano, M.; El Kissi, N.; Dufresne, A. Cellulose nanocrystals and related nanocomposites: Review of some properties and challenges. *Journal of Polymer Science Part B: Polymer Physics* **2014**, *52*, 791–806, https://doi.org/10.1002/polb.23490.
40. Rhim, T.; Lee, D.Y.; Lee, M.J. Hypoxia as a target for tissue specific gene therapy. *Control Release* **2013**, *172*, 484–494, https://doi.org/10.1016/j.jconrel.2013.05.021.
41. Trache, D.; Tarchoun, A.F.; Derradji, M.; Hamidon, T.S.; Masruchin, N.; Brosse, N.; Hussin, M.H. Nanocellulose: from fundamentals to advanced applications. *Frontiers Chemistry* **2020**, *8*, 392-405, https://doi.org/10.3389/fchem.2020.00392.
42. Bielejewska, N.; Hertmanowski, R. Functionalization of LC molecular films with nanocrystalline cellulose: a study of the self-assembly processes and molecular stability. *Colloids and Surfaces B Biointerfaces* **2020**, *187*, 110634, https://doi.org/10.1016/j.colsurfb.2019.110634.

43. Akhlaghi, M.A.; Bagherpour, R.; Kalhori, H. Application of bacterial nanocellulose fibers as reinforcement in cement composites. *Construction and Building Materials* **2020**, *241*, 118061, https://doi.org/10.1016/j.conbuildmat.2020.118061.
44. Balea, A.; Fuente, E.; Monte, M.C.; Merayo, N.; Campano, C.; Negro, C.; Blanco, A. Industrial Application of nanocelluloses in papermaking: a review of challenges, technical solutions, and market perspectives. *Molecules* **2020**, *25*, 526-534, https://doi.org/10.3390/molecules25030526.
45. Charreau, H.; Cavallo, E.; Foresti, M.L. Patents involving nanocellulose: analysis of their evolution since 2010. *Carbohydrate Polymers* **2020**, *237*, 116039, https://doi.org/10.1016/j.carbpol.2020.116039.
46. Huang, X.; Panahi-Sarmad, M.; Dong, K.; Li, R.; Chen, T.; Xiao, X. Tracing evolutions in electro-activated shape memory polymer composites with 4D printing strategies: A systematic review. *Composites Part A: Applied Science and Manufacteuring* **2021**, *147*, 106444, https://doi.org/10.1016/j.compositesa.2021.106444.
47. Cazón, P.; Velazquez, G.; Vázquez, M. Characterization of mechanical and barrier properties of bacterial cellulose, glycerol, and polyvinyl alcohol (PVOH) composite films with eco-friendly UV-protective properties. *Food Hydrocolloids* **2020**, *99*, 105323, https://doi.org/10.1016/j.foodhyd.2019.105323.
48. Tibolla, H.; Czaikoski, A.; Pelissari, F.M.; Menegalli, F.C.; Cunha, R.L. Starch-based nanocomposites with cellulose nanofibers obtained from chemical and mechanical treatments. *International Journal of Biological Macromolecules* **2020**, *161*, 132–146, https://doi.org/10.1016/j.ijbiomac.2020.05.194.
49. Abral, H.; Ariksa, J.; Mahardika, M.; Handayani, D.; Aminah, I.; Sandrawati, N.; Sapuan, S.M.; Ilyas, R.A. Highly transparent and antimicrobial PVA based bionanocomposites reinforced by ginger nanofiber. *PolymerTesting* **2020**, *81*, 106186, https://doi.org/10.1016/j.polymertesting.2019.106186.
50. Zainal, S.H.; Mohd, N.H.; Suhaili, N.; Anuar, F.H.; Lazim, A.M.; Othaman, R. Preparation of cellulose-based hydrogel: a review. *Journal of Materials Research Technology* **2021**, *10*, 935-952, http://dx.doi.org/10.1016/j.jmrt.2020.12.012.
51. Cheng, M.; Qin, Z.; Hu, J.; Liu, Q.; Wei, T.; Li, W. Facile and rapid one–step extraction of carboxylated cellulose nanocrystals by H2SO4/HNO3 mixed acid hydrolysis. *Carbohydrate Polymers* **2020**, *231*, 115701, https://doi.org/10.1016/j.carbpol.2019.115701.
52. Dai, L.; Wang, Y.; Zou, X.; Chen, Z.; Liu, H.; Ni, Y. Ultrasensitive physical, bio, and chemical sensors derived from 1, 2, and 3-D nanocellulosic materials. *Small* **2020**, *16*, 1906567, https://doi.org/10.1002/smll.201906567.
53. Dominic, M.; Joseph, R.; Begum, P.S.; Kanoth, B.P.; Chandra, J.; Thomas, S. Green tire technology: effect of rice husk derived nanocellulose (RHNC) in replacing carbon black (CB) in natural rubber (NR) compounding. *Carbohydrate Polymers* **2020**, *230*, 115620, https://doi.org/10.1016/j.carbpol.2019.115620.
54. Gan, P.; Sam, S.; Abdullah, M.F.; Omar, M.F. Thermal properties of nanocellulose-reinforced composites: a review. *Journal of Applied Polymer Science* **2020**, *137*, 48544, https://doi.org/10.1002/app.48544.
55. Gao, H.; Sun, Q.; Han, Z.; Li, J.; Liao, B.; Hu, L.; Huang, J.; Zou, C.; Jia, C.; Huang, J.; Chang, Z.; Jiang, D.; Jin, M. Comparison of bacterial nanocellulose produced by different strains under static and agitated culture conditions. *Carbohydrate Polymers* **2020**, *227*, 115323, https://doi.org/10.1016/j.carbpol.2019.115323.
56. Cheng, H.; Xu, H.; McClements, D.J.; Chen, L.; Jiao, A.; Tian, Y.; Miao, M.; Jin, Z. Recent advances in intelligent food packaging materials: Principles, preparation and applications. *Food Chemistry* **2021**, *375*, 131738, https://doi.org/10.1016/j.foodchem.2021.131738.
57. Alizadeh-Sani, M.; Tavassoli, M.; Mohammadian, E.; Ehsani, A.; Khaniki, G.J.; Priyadarshi, R.; Rhim, J.W. pH-responsive color indicator films based on methylcellulose/chitosan nanofiber and barberry anthocyanins for real-time monitoring of meat freshness. *International Journal of Biological Macromolecules* **2021**, *166*, 741–750, https://doi.org/10.1016/j.ijbiomac.2020.10.231.
58. Hazrati, K.; Sapuan, S.; Zuhri, M.; Jumaidin, R. Preparation and characterization of starch-based biocomposite films reinforced by Dioscorea hispida fibers. *Journal Materials Research and Technology* **2021**, *15*, 1342–1355, https://doi.org/10.1016/j.jmrt.2021.09.003.
59. Khouaja, A.; Koubaa, A.; Ben Daly, H. Dielectric properties and thermal stability of cellulose high-density polyethylene bio-based composites. *Industrial Crops and Products* **2021**, *171*, 113928, https://doi.org/10.1016/j.indcrop.2021.113928.
60. Filho, G.R.; de Assuncao, R.M.M.; Vieira, J.G.; Meireles, C.D.S.; Cerqueira, D.A.; Barud, H.D.S.; Ribeiro, S.J.L.; Messaddeq, Y. Characterization of methylcellulose produced from sugar cane bagasse cellulose:

crystallinity and thermal properties. *Polymer Degradation and Stability* **2007**, *92*, 205–210, https://doi.org/10.1016/j.polymdegradstab.2006.11.008.
61. Khan, R.A.; Salmieri, S.; Dussault, D.; Calderon, J.; Kamal, M.R.; Safrany, A.; Lacroix, M. Production and properties of nanocellulose-reinforced methylcellulose-based biodegradable films. *Journal of Agricultural and Food Chemistry* **2010**, *58*, 7878–7885, https://doi.org/10.1021/jf1006853.
62. Poletto, M.; Ornaghi, H.L., Júnior; Zattera, A.J. Native cellulose: structure, characterization and thermal properties. *Materials* **2014**, *7*, 6105–6119, https://doi.org/10.3390/ma7096105.
63. Reddy, J.P.; Rhim, J.W. Characterization of bionanocomposite films prepared with agar and paper-mulberrypulp nanocellulose. *Carbohydrate Polymers* **2014**, *110*, 480–488, https://doi.org/10.1016/j.carbpol.2014.04.056.
64. Li, Q.Q. Nanocellulose: preparation,characterisation,supramolecular modelling and its life cycle assessment. *Virginia Technology* **2012**, 1–169.
65. Lee, K.Y.; Aitomäki, Y.; Berglund, L.A.; Oksman, K.; Bismarck, A. On the use of nanocellulose as reinforcement in polymer matrix composites. *Composites Science and Technology* **2014**, *105*, 15–27, https://doi.org/10.1016/j.compscitech.2014.08.032.
66. Poletto, M.; Zattera, A.J.; Santana, R.M.C. Structural differences between wood species: evidence from chemical composition, FTIR spectroscopy, and thermogravimetric analysis. *Journal of Applied Polymer Science* **2012**, *26*, 336–343, https://doi.org/10.1002/app.36991.
67. Bridarolli, A.; Odlyha, M.; Nechyporchuk, O.; Holmberg, K.; Ruiz-Recasens, C.; Bordes, R.; Bozec, L. Evaluation of the adhesion and performance of natural consolidants for cotton canvas conservation. *ACS Applied Materials & Interfaces* **2018**, *10*, 33652–33661, https://doi.org/10.1021/acsami.8b10727.
68. Nechyporchuk, O.; Kolman, K.; Bridarolli, A.; Odlyha, M.; Bozec, L.; Oriola, M.; Campo-Francés, G.; Persson, M.; Holmberg, K.; Bordes, R. On the potential of using nanocellulose for consolidation of painting canvases. *Carbohydrate Polymers* **2018**, *194*, 161–169, https://doi.org/10.1016/j.carbpol.2018.04.020.
69. Ng, H.M.; Sin, L.T.; Bee, S.T.; Tee, T.T.; Rahmat, A.R. Review of nanocellulose polymer composite characteristics and challenges. *Polymer-Plastics Technology and Engineering* **2017**, *56*, 687–731, https://doi.org/10.1080/03602559.2016.1233277.
70. Peresin, M.S.; Habibi, Y.; Vesterinen, A.H.; Rojas, O.J.; Pawlak, J.J.; Seppala, J.V. Effect of moisture on electrospun nanofiber composites of polyvinyl alcohol and cellulose nanocrystals. *Biomacromolecules* **2010**, *11*, 2471–2477, https://doi.org/10.1021/bm1006689.

Supplementary material

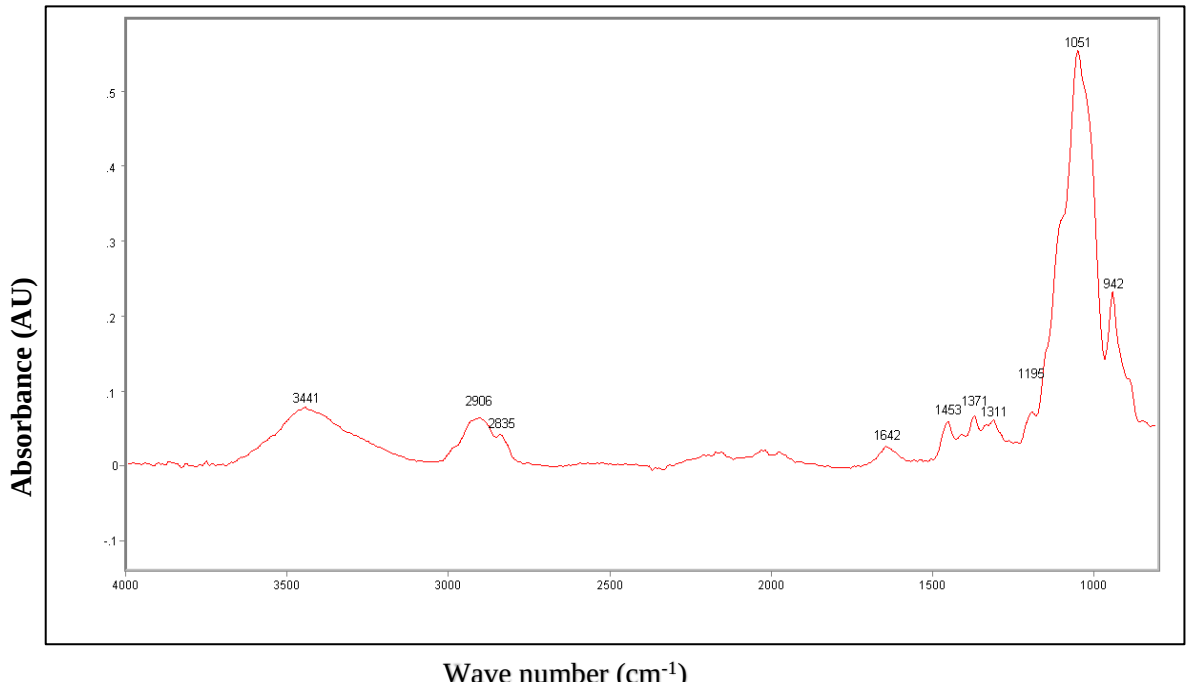

Figure S1. FTIR spectra of Tylose MH 50 (1.5%, w/w) based film (control) of batch- P 27.7.17.

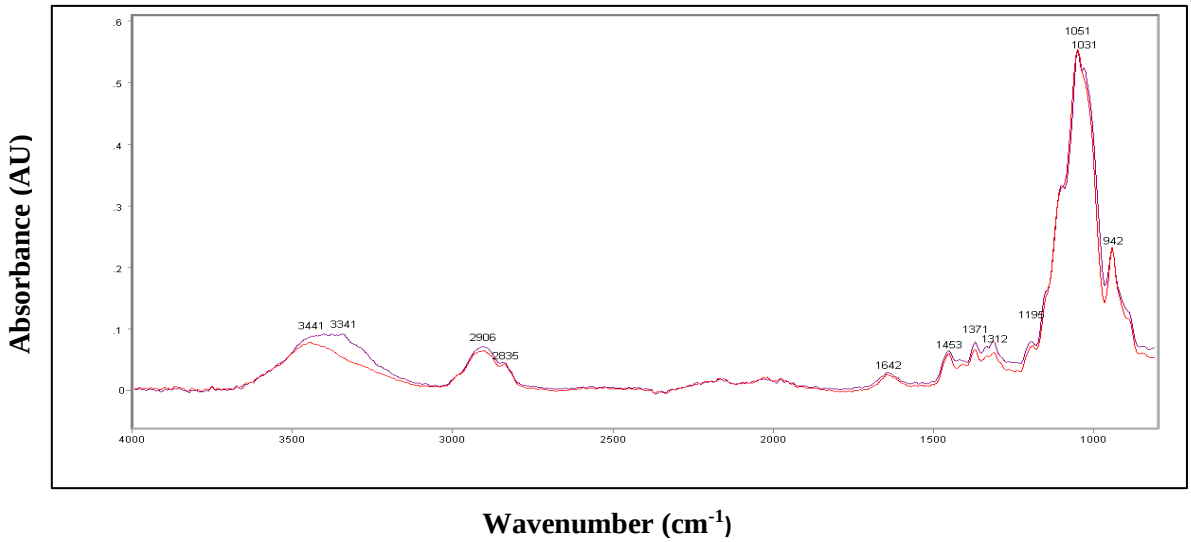

Figure S2. FTIR spectra of Tylose MH 50 (1.5%, w/w) (red) and Tylose MH 50+15% CNC (w/w) (purple) composite films of batch-1 (P 27.7.17).

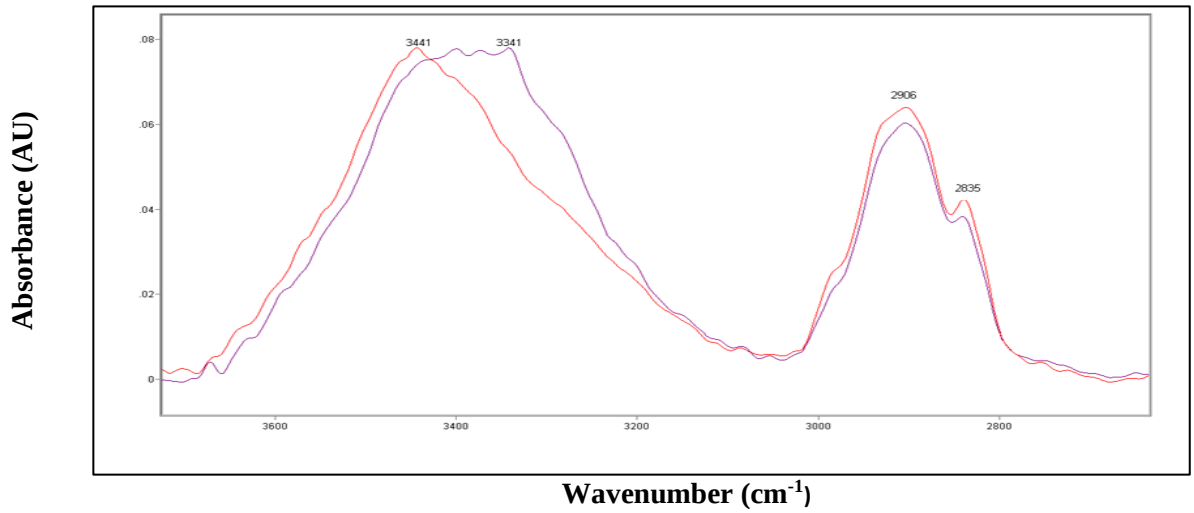

Figure S3. Spectral region at 2700-3700 cm^{-1} of Tylose MH 50(1.5%)(w/w) (red) and Tylose+15% CNC (w/w) (purple) composite films of batch 1 (P 27.7.17).

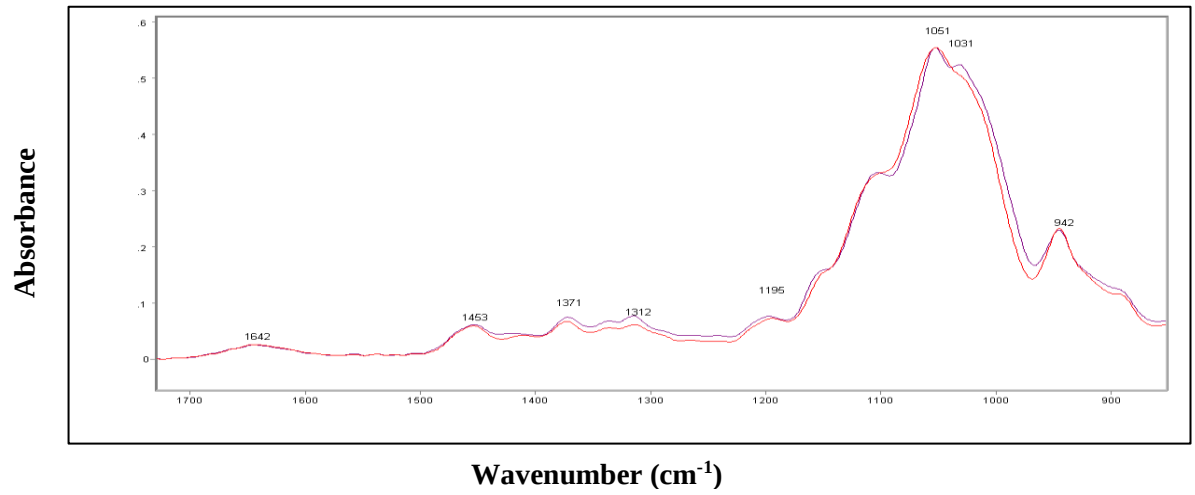

Figure S4. FTIR spectra in the region from 800-1800 cm^{-1} of Tylose MH 50(1.5%, w/w) (red) and Tylose MH 50+15% CNC (w/w) (purple) composite films of batch 1 (P 27.7.17).